



In-situ mechanical investigation of the deformation of splat interfaces in cold-sprayed aluminum alloy



Pranjal Nautiyal^a, Cheng Zhang^a, Victor K. Champagne^b, Benjamin Boesl^a, Arvind Agarwal^{a,*}

^a Plasma Forming Laboratory, Florida International University, 10555 West Flagler Street, Miami, FL 33174, USA

^b US Army Research Laboratory, Weapons and Materials Research Directorate, Aberdeen Proving Ground, Aberdeen, MD 20783, USA

ARTICLE INFO

Keywords:

Cold spray
Mechanical properties
Splat sliding
Multiscale mechanics
In-situ investigation

ABSTRACT

The mechanical properties of cold sprayed deposits, with splats as their building blocks, are affected by debonding and relative sliding of splats during mechanical loading. In this study, inter-splat deformation behavior in 6061 Al coatings is investigated by *in-situ* mechanical characterization for real-time visualization. The role of processing gas type (He vs. Air), splat geometry, particle bonding, and post-spray heat treatment on splat sliding is evaluated. High porosity and poor splat-bonding in air-sprayed coating result in inferior microhardness (917 MPa) and flexural strength (120 MPa), as compared to He-sprayed coating which exhibits microhardness and flexural strength of 1000 MPa and 450 MPa, respectively. *In-situ* cyclic bending of coatings is performed inside a scanning electron microscope to examine the splat deformation behavior. Digital image correlation (DIC) analysis of the real-time videos is performed to determine local microstructure strains, experimentally demonstrating splat sliding phenomenon for the first time. Heat-treatment of the coatings heals inter-splat microcracks, reduces porosity and consequently improves the mechanical properties. DIC strain maps revealed arrested splat sliding after heat-treatment. A splat sliding factor (SS_f) is introduced, which compares cold-sprayed microstructure deformation with the bulk structure like substrate, providing quantitative information about inter-splat bonding. The SS_f is found to be higher for air-sprayed coating (~1.4) as compared to He-sprayed coating (~0.28), and is further reduced after heat-treatment. The correlation between splat sliding and microstructure will enable development of coatings with predictable and improved mechanical properties by cold spray.

1. Introduction

Cold spray has emerged as a promising surface engineering and additive manufacturing process for depositing metallic powder particles in the solid state, forming dense metallic deposits with relatively low oxide content and superior inter-particle adhesion [1–7]. The powder particles are introduced in a hot process gas (Helium, Nitrogen, or Air) and accelerated to supersonic velocities before they impact upon a substrate to form a deposit. The complex thermodynamic and mechanical phenomena involved in the deposition process lead to a hierarchical microstructure [1]. If the critical impact velocity of the accelerating particles is attained upon impact, the solid particles deform and create a bond with the substrate [8–10]. Adequate velocity is necessary for optimal particle consolidation and coating density. Several important process parameters, such as the pressure and temperature of the gas and particles, particle characteristics, and nozzle geometry affect the particle velocity. The particle impact results in a high intensity

pressure wave [3] and the material undergoes severe plastic deformation that is concentrated in a narrow region surrounding the particle/substrate and particle/particle interface. Most notably, the outer contact regions of the impacting particle experience excessive strains (as high as 1000%) and the material loses its ability to resist shear flow, resulting in the formation and ejection of material jet [1,3]. This jetting phenomenon disrupts the oxide layers on both the powder particles and/or substrate and leads to an intimate contact between the particles by exposing ‘clean’ metal surfaces [11], which aids in the formation of a metallurgical bond [12,13]. It has been deduced based upon empirical evidence that both metallurgical bonding, in combination with mechanical interlocking, serve as the predominant bonding mechanisms in cold spray, and under certain high process parameter settings for main gas temperature and pressure, melting can be observed [14,15].

The deformed, deposited and bonded particles are the fundamental building blocks of the cold spray deposits and are called as splats. High strain rate, rapid heating/cooling and localized pressure can induce

* Corresponding author.

E-mail address: agarwala@fiu.edu (A. Agarwal).

dynamic recrystallization along the splat boundaries, resulting in ultra fine-grained microstructure at particle interfaces [16–19]. Contrary to this, the interior region of the splat comprises of larger micron-sized grains due to much lower strains ($\epsilon < 1$) and localized temperatures compared to the splat boundaries [20]. This results in non-uniform distribution of mechanical properties in a splat. Nanoindentation studies reveal higher nanohardness along the splat boundaries that directly impact upon the already deposited particles, and is associated with localized work hardening during deposition [18,20–22]. For instance, particle boundary in a 6061 Al coating is characterized by a nano-hardness of 1.77 GPa, as against a hardness of 1.43 GPa for particle interior [18]. Even the splat boundaries can exhibit heterogeneous mechanical properties, depending on the local thermo-mechanical phenomena. Goldbaum and co-workers observed that jetting region of the splat boundary has a lower hardness (3.2–3.4 GPa), compared to impact region (3.7–4.2 GPa) [22]. This is attributed to thermal softening associated with jetting. Therefore, the variation in the degree of cold working and thermal softening can result in heterogeneous splat boundary microstructure and mechanical properties. Chemical segregation can also contribute to differences in mechanical properties in the micron-sized 6061 Al powder particles produced by gas atomization process.

The bulk deformation of the cold sprayed structures is not only influenced by the gradation of mechanical properties in a single splat, but also the variation in the bonding between the splats. While the peripheral region of the impacting particle is strongly bonded with the substrate/ adjacent particle due to jetting, the central region of the impacting particle interface is relatively weakly bonded due to the lack of sufficient shear flow to induce bonding. Relatively lower temperatures are not high enough to induce localized metallurgical bonding [1]. These weak inter-splat boundaries act as crack nuclei, leading to material failure at critical loads [18,23,24]. For applied loads below the failure point, the splats can de-bond and slide past each other as the deposit is deformed, limiting the material's ability to resist plastic deformation. This phenomenon is known as 'Splat Sliding' [25,26] (schematically shown in Fig. 1a). The current understanding of this relative sliding motion between the splats in a coating microstructure is very limited. Chen and co-workers used indentation approach to induce localized stresses in a plasma sprayed Al-Si alloy coating and modeled the inter-splat friction force in the elasto-plastic deformation region under the indenter tip [26]. A very small friction force (of the order of 10^{-4} N) was computed between the splats, and it was hypothesized that easy activation of splat sliding in the coating is responsible for the loss in the elastic modulus (compared to the theoretical elastic modulus of the alloy). Inter-splat deformation behavior is expected to be more complicated in cold sprayed coatings due to heterogeneity in the microstructure along the splat boundaries, with either highly cold-worked interfaces characterized by high dislocation densities or recrystallized interfaces consisting of ultrafine grains [16,27,28]. Fractography studies have revealed that cold spray deposits can be susceptible to inter-splat delamination and crack propagation along the particle boundaries [12,29]. This often results in low ductility of cold sprayed structures [18,30]. A recent study reported the impressive tensile strength of cold sprayed 6061 Al coatings (~460 MPa), but the ductility was low (only about 3%) as compared to wrought materials [18], which is undesirable for structural applications due to the possibility of catastrophic in-service failure. This necessitates a deeper understanding of the effect of processing and microstructure on inter-splat mechanics in cold sprayed metallic coatings.

In this study, *in situ* approach is used for studying the deformation behavior of cold sprayed microstructure. 6061 Al, which is an important aerospace and defense alloy, is cold sprayed using Helium and air as the processing gases. These two specimens are subjected to flexural bending under a scanning electron microscope (SEM) to examine the deformation of the coatings in real time. Digital Image Correlation (DIC) analysis approach is used to quantify the localized

microstructure strains developed in the coating during deformation, providing critical information about inter-splat mechanics. Additionally, effect of post-spray heat treatment on microstructure and mechanics of the coatings is examined. Some of the key fundamental questions that this work seeks to answer are:

- How the individual splat characteristics/ mechanics is related with the overall coating deformation characteristics?
- How the nature and strength of inter-splat bonding affects the mechanical properties?
- What is the correlation between microstructure and degree of mechanical isotropy/ anisotropy in cold-sprayed coatings?
- What is the influence of varying degrees of plastic deformation of the particles (during deposition) and solid-state diffusion (during post-spray heat-treatment) on the mechanics of the coatings?

Real-time investigation of the splat mechanics is much needed for a clear understanding of the interrelationship between mechanical properties of coatings, splat characteristics, and inter-particle bonding. These insights into processing-microstructure-property correlation are useful for developing cold-sprayed coatings with predictable properties, which is the prime motivation of this study. *In-situ* mechanics is a powerful approach to decode deformation behavior in complex hierarchical and heterogeneous cold sprayed microstructures.

2. Experimental details

2.1. Processing and microstructure characterization

Gas atomized 6061 Al powder particles with an average size of 38.7 μm (Valimet, CA, USA) were cold sprayed on polished and cleaned 6061-T6 Al substrate. The coatings were developed using a high-pressure CGT 4000 cold spray system (CGT Technologies, Munich, Germany) under two sets of spraying conditions: (i) air as the carrier gas while maintaining a pressure of 6.2 MPa and a temperature of 451 °C at the gun, and (ii) He as the carrier gas with pressure and temperature at the gun as 3.45 MPa and 384.3 °C, respectively. *The objective of using these two different process conditions was to obtain coatings with significantly different microstructures (porosity, splat geometry, interface bonding and degree of cold working).* The key motive of this study is to understand how mechanics and microstructure of cold-sprayed coatings are correlated.

The top surface of the deposited coatings was examined under a JEOL JSM-6330F field emission SEM (Tokyo, Japan). The coatings were sectioned, mounted, ground and polished to observe the cross-sectional microstructure. The SEM imaging was performed at an operating voltage of 30 kV and a working distance of 15–20 mm. Image analysis was performed to measure coating porosity.

2.2. Post-spray heat treatment

The coatings were subjected to 176 °C for 1 h (stress relief condition) [18]. Stress relief condition is a common commercial heat-treatment for 6061 Al. The treatment was performed in Argon atmosphere to prevent oxidation. The effect of heat treatment on microstructure and mechanical deformation of the coatings was examined.

2.3. Mechanical investigations

In order to correlate the mechanics of splats and interfaces with the overall coating mechanics, the mechanical properties were evaluated at multiple length scales: nanoindentation modulus mapping for localized response of splats and interfaces, microhardness to capture the aggregate response of multiple splats and interfaces, and flexural characterization to assess the mechanical deformation/ failure of the overall coating.

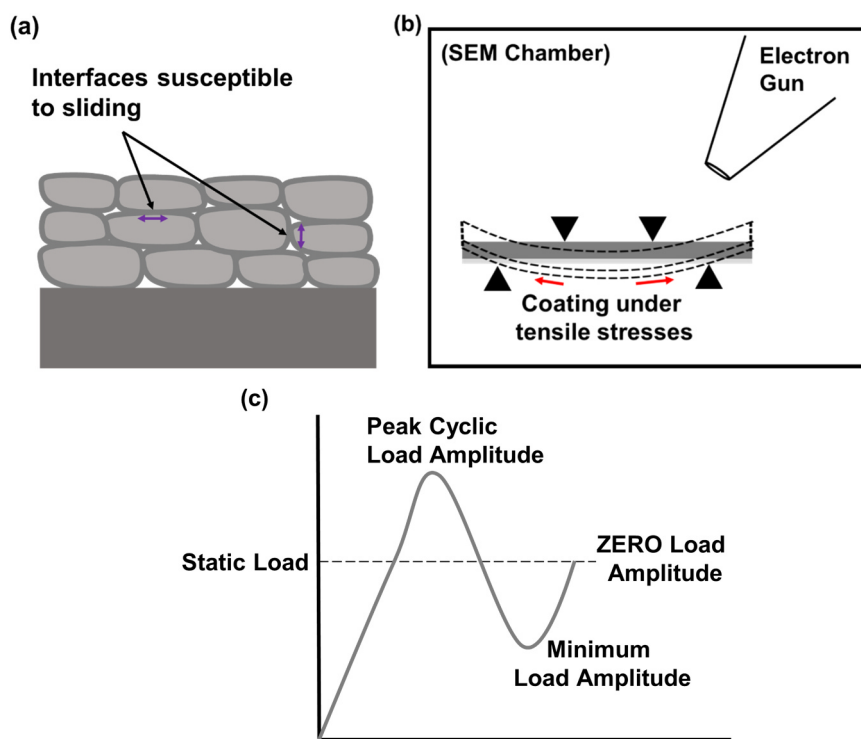


Fig. 1. (a) Schematic representation of splat interfaces susceptible to sliding in cold sprayed coatings. (b) Schematic representation of the specimen subjected to four-point bending inside the SEM chamber, with cold-sprayed coating experiencing tensile stresses. (c) Nature of cyclic flexural load profile.

2.3.1. Scanning probe microscopy-nanoindentation modulus mapping

Nature of inter-splat bonding was probed by scanning probe microscopy (SPM) and modulus mapping of the cross-section of the polished coatings using TI 900 Triboindenter (Hysitron Inc., Minneapolis, USA). SPM imaging closely captures the topography, providing accurate information about the inter-splat pores. The imaging was performed before and after heat-treatment, to study the effect of solid-state diffusion on microstructure evolution. SPM imaging was complemented by nanoindentation modulus mapping, to obtain the spatial distribution of the elastic modulus, aiding in evaluating porosities along splat boundaries. A diamond Berkovich tip of 100 nm diameter was used to indent a $50 \mu\text{m} \times 50 \mu\text{m}$ area in both the coatings. In modulus mapping, a static load is applied by the indenter tip on the specimen surface, which is superimposed by a dynamic loading-unloading cycle [31]. The static and dynamic loads applied to the coatings were 2 μN and 0.5 μN , respectively. The frequency of the dynamic loading was 200 Hz.

2.3.2. Microhardness

Microhardness values were obtained by performing indentations using LECO LM810AT microhardness tester (LECO Corp., St. Joseph, USA) on the polished cross-section of the coatings. At least 10 indents, with an applied force of $\sim 490 \text{ mN}$, were made on each sample.

2.3.3. Flexural testing

Flexural strength of the coatings was determined by performing four-point bending tests using MTI SEMtester (Albany, USA) with special custom-developed fixtures. The specimens were mounted such that the coating experiences tensile stresses during the bending deformation, schematically shown in Fig. 1b. The coatings were rectangular in shape (length = 30 mm, width = 5 mm and thickness = 3.8 mm, such that the substrate and the coating are 3 mm and 0.8 mm thick, respectively). All the coatings were ground before the mechanical testing to a similar thickness of 800 μm . The failure of the coatings was optically captured and recorded by Dino-Lite AM2111 digital microscope (New Taipei City, Taiwan). The videos are provided in the supplementary information (Video V1 and Video V2).

Supplementary material related to this article can be found online at doi:10.1016/j.jssc.2018.09.022.

In situ bending deformation of the coatings was performed inside a dual beam JEOL JIB-4500 focused ion beam/SEM system, and real-time videos of microstructure deformation were captured. These tests were performed below the failure point, in elastic/plastic deformation regime. The coatings were subjected to a static applied load of 200 N (which corresponds to 50% of the failure point for air-sprayed coating), superimposed by a cyclic load amplitude of $\pm 100 \text{ N}$ (Fig. 1c).

2.4. Digital image correlation analysis

Insights into microstructure deformation were developed by performing strain analysis of the real-time deformation snapshots using VIC-2D digital image correlation (DIC) software (Correlated Solutions, Irmo, USA). In DIC analysis, the real-time snapshots of the microstructure (during deformation) are compared/analyzed with respect to the starting snapshot, to capture the changes in specimen surface incrementally as the force is applied [32]. The software tracks and correlates the pixels in the deformed snapshots with respect to the starting image. This relative comparison aids in determining full field 2D strain map, showing spatial distribution of strains in the microstructure as a function of mechanical loading [33]. Compared to physical strain measurement techniques (using gages), visual image correlation has numerous advantages, such as easy set-up, ability to determine strains for much complex deformation state in 4-point bending and excellent spatial resolution, providing strain distribution over the entire microstructure. As a result, DIC is a powerful, time-efficient technique to probe deformation characteristics of different features in the microstructure. Ability to capture all this information by performing a single test is otherwise not possible using physical strain gages.

In this study, DIC analysis of high-resolution SEM snapshots was performed to evaluate strains in the splats and interfaces, providing insights into microstructure deformation mechanisms in cold-sprayed coatings. Strain maps with local strain contours were obtained, superimposed on the real-time SEM images, providing quantitative

information about splat deformation. Therefore, while *in-situ* SEM videos are merely qualitative, the superimposed DIC maps on the real time snapshots provides quantitative information about deformation. The DIC videos of the air and He-sprayed coatings are provided as supplementary information (Videos V3-V5). These videos show microstructure strain evolution during the 4-point bending loading/unloading/reloading cycle. The strains obtained by DIC analysis were plotted as a function of time, and compared for different processing and post-processing conditions. Additionally, strains in the coatings in x- and y-directions (perpendicular and parallel to spray direction) were determined by DIC to assess the degree of isotropy/ anisotropy in the cold-sprayed microstructures.

Supplementary material related to this article can be found online at doi:10.1016/j.jssc.2018.09.022.

3. Results and discussion

3.1. Coating microstructure

Fig. 2 shows the SEM micrographs of the top surface of the deposited coatings. Plastic deformation due to high-velocity impact in cold spray leads to flattening of particles. The extent of deformation in air-sprayed particles (**Fig. 2a**) is limited, as against the He-sprayed particles which show remarkable flattening and densification (**Fig. 2b**). The ratio of particle diameters after and before impacts is known as mean flattening ratio, and it is proportional to the particle strain [34]. The flattening ratio of the air and He-processed coatings were computed to be 1.04 and 1.6, respectively. A closer examination of splat boundaries reveals extensive jetting in He-sprayed coating, as shown in **Fig. 2d**. This produces intimate metal-metal contact, ideal for metallurgical bonding between the splats. Contrary to this, jetting does not appear to be prominent in the air-sprayed coating (**Fig. 2c**). Because of lower deformability and limited jetting of air-sprayed particles, the interfaces are weakly bonded and characterized by porosities as shown in **Fig. 2c**. Low degree of flattening results in globular splat structure in the air-sprayed coating, as shown in **Fig. 3a**. On the other hand, He-sprayed microstructure comprises of parachute-shaped elongated particles (**Fig. 3b**). Heavy plastic deformation leads to the formation of a dense and tightly-bonded coating with very low porosity (~ 0.8%), as the impacting particles can readily conform to the deposited layer by local plastic deformations along splat boundaries (**Fig. 3b**). On the other hand, air-sprayed particles did not deform significantly, resulting in marked porosity ~ 4.5% (**Fig. 3a**).

3.2. Mechanical properties

3.2.1. Bulk deformation characteristics

The coatings were indented using Vickers tip to characterize the plastic deformation behavior. A gradation in plastic response was observed: the microhardness gradually decreased as the distance from the substrate increased. The air-sprayed coating exhibited microhardness values varying from 962 MPa near the substrate to 888 MPa towards the top of the coating. The microhardness values were higher for He-sprayed coating, with the highest value near the substrate to be 1016 MPa, and ~ 988 MPa towards the top of the coating. Relatively inferior indentation resistance of the air-sprayed coating can be ascribed to high porosity in the coating. Many of the splat interfaces are weakly bonded, as shown in the SEM micrograph in **Fig. 3a**. As a result, localized stresses induced by the indenter tip can de-bond, delaminate and cause sliding of the splats [26], resulting in inferior resistance to deformation.

To examine the failure characteristics, the coating was subjected to four-point bending test, and the deformation was recorded by an optical camera. The motive of evaluating four-point bending behavior is to allow crack propagation through the coating until it reaches the substrate. This provides two vital information: first, the deformation of the

coatings, and second, the delamination at coating/ substrate interface. The air-sprayed coating failed at 120 MPa and was characterized by a high degree of brittleness (less than 0.4 mm deflection). The sudden drop in the stress-deflection plot of the coating in **Fig. 4** (encircled) is the failure point. The failure was abrupt at that point and was observed under the optical camera (Supplementary Video V1). There was rapid crack propagation vertically from the coating to the substrate. It was followed by delamination of the coating at the substrate-coating interface. The optical snapshots of the failed and delaminated coatings are shown as the insets in **Fig. 4**. The He-sprayed coating was found to exhibit much higher flexural strength of ~ 450 MPa as compared to the air-sprayed coating. It can be seen from the stress-deflection plot that the ductility is also remarkably higher than air-processed coating, as the deflection to failure exceeds 1.5 mm. There is limited delamination from the substrate, suggesting strong adhesion (inset of **Fig. 4**). Supplementary Video V2 shows less abrupt failure and higher plasticity of the He-sprayed coating. As observed in **Fig. 2d**, the He-sprayed coating exhibits extensive jetting, which can lead to localized melting, thermal softening, grain recrystallization and metallurgical bonding between the particles [22]. This results in superior ductility. On the other hand, limited jetting observed in the air-sprayed coating (**Fig. 2a** and **c**) does not allow thermal relief and weakly bonded porous particle interfaces act as crack nuclei and pathways for cracks to propagate. Hence, air-sprayed coating fails abruptly and is brittle. It is noteworthy that the stress-deflection plot in **Fig. 4** represents the combined mechanical response of the coating as well as the substrate. However, since the substrate material and thickness was maintained constant in both the bi-layer specimens, the curves provide good comparison of properties of the two cold-sprayed coatings with varied microstructures.

3.2.2. Microstructure strain evolution

Both air-sprayed and He-sprayed coatings were subjected to cyclic four-point bending test inside a SEM chamber, and the real-time videos were captured. DIC analysis of the real-time snapshots provided information about the strain development in the coating microstructures. **Fig. 5a** shows the microstructure strain evolution during the cyclic loading. A static load of 200 N was applied to the coating, and it was superimposed with a ± 100 N dynamic load amplitude. It should be noted that the coating is under tensile stresses during the loading/unloading/reloading cycle, as shown in **Fig. 1b**. The figure shows x and y-direction strain development in the coating as a function of time, where the y-axis is along the cold spray direction, and x is perpendicular to the spraying direction. There is very little anisotropy in the strain values in x and y-directions, and this can be related to the fact that air-processed coating comprised of globular splats (**Fig. 3a**), with a small flattening ratio of 1.04. It can be seen that the micro-strain value increases or decreases as a function of the direction of application of the dynamic load. A maximum amplitude, which is + 100 N applied dynamic load results in net microstrains as high as ~ 1.8. A minimum microstrain of ~ - 0.5 was recorded for the minimum applied load amplitude (- 100 N). The microstructure deformation is not 100% reversible, as evidenced by different absolute values of strains for the maximum (+ 100 N) and minimum load amplitudes (- 100 N). When the cyclic tests ended and the applied dynamic load was 0 N, a residual or permanent microstructure strain is observed (**Fig. 5a**).

The DIC strain maps of the coating at maximum, minimum and zero load amplitudes are shown in **Fig. 5b**, c, and d, respectively. The maps are superimposed on the SEM micrograph of the area of the coating that was being imaged during the test. The different color contours represent different microstructure strain regimes developed in the coating, and the color code of the contours is provided on the right-hand side of each strain map. It is noteworthy that the strain plot of **Fig. 5(a)** represents the ‘average value’ of the local contour strains in the SEM image at each time instant. Hence, we term it as the microstructure strain (labeled as microstrain in **Fig. 6a**). It is interesting to observe that there are both negative and positive strain contours; the

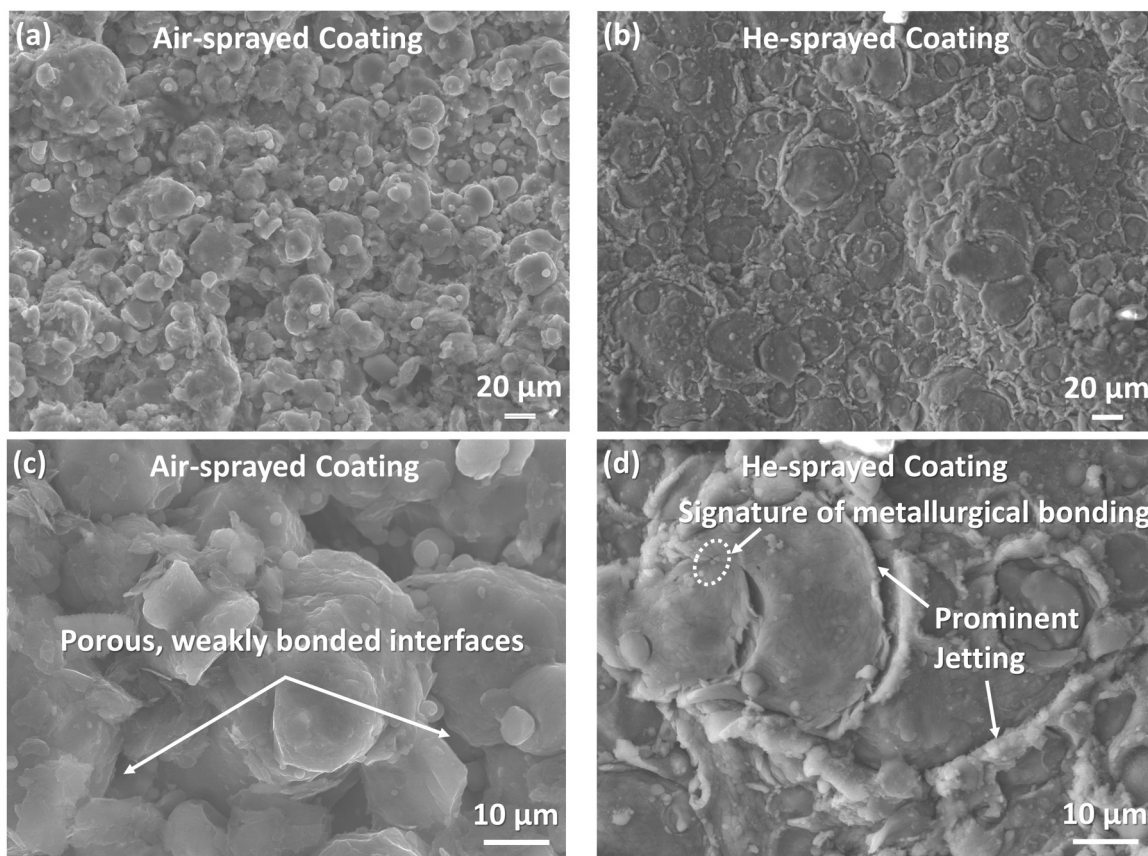


Fig. 2. SEM micrographs of as-deposited top surfaces of: (a) Air-sprayed coating, and (b) He-sprayed coating. Higher magnification SEM micrographs of the splats and splat interfaces are shown for (c) air-sprayed coating and (d) He-sprayed coating.

white arrows drawn on the contours indicate the net direction of strain or deformation. The maps reveal a complex deformation pattern, with relative sliding between the splats. The presence of positive and negative contours suggests that during load application, the coating microstructure does not deform as a single rigid unit. Rather, there is relative sliding along the splat interfaces. This is a major finding, and for the first time validates Splat Sliding in thermal/cold sprayed microstructures. Supplementary Video V3 shows the evolution of strain over time in the Air-sprayed coating. It should be noted that the strain-time plot in Fig. 5a provides the net microstructure strain evolution over time, whereas the strain maps in Fig. 5b-d provide spatial distribution of strains in the cold-sprayed microstructure at a given instant.

The microstructure deformation of the He-processed coating was

also examined for similar load conditions (Supplementary Video V4). Unlike the air-sprayed coating, the He-sprayed coating was found to exhibit a very high degree of anisotropy regarding x and y-direction strains as plotted in Fig. 6a. The deformation along the y-direction (i.e., spray direction) is highly restricted, with lower values of local strain. The DIC strain maps for the x and y-direction deformation at the peak amplitude point (+ 100 N) are compared in Fig. 6b and c, respectively. While the local contour strain in the x-direction (ϵ_x) is found to be as high as 4.15, the maximum value of local contour strain in the y-direction (ϵ_y) is only 1.96. In addition to the magnitude of the strain values, there is also a marked difference in the nature of strain contours. The strain distribution is not as heterogeneous in the y-direction (Fig. 6c), as it is for x-direction (Fig. 6b). The number of interfaces that

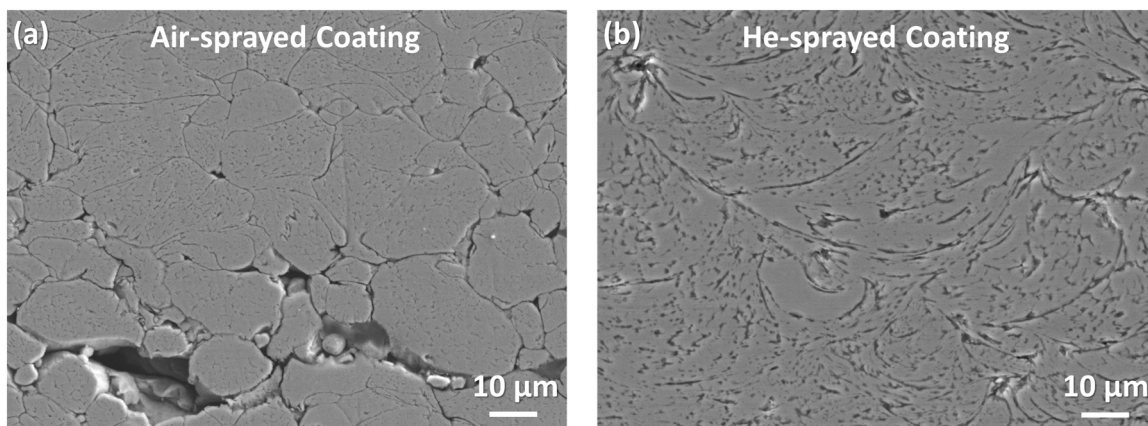


Fig. 3. SEM micrographs of polished and etched cross-sections of: (a) Air-sprayed coating, and (b) He-sprayed coating.

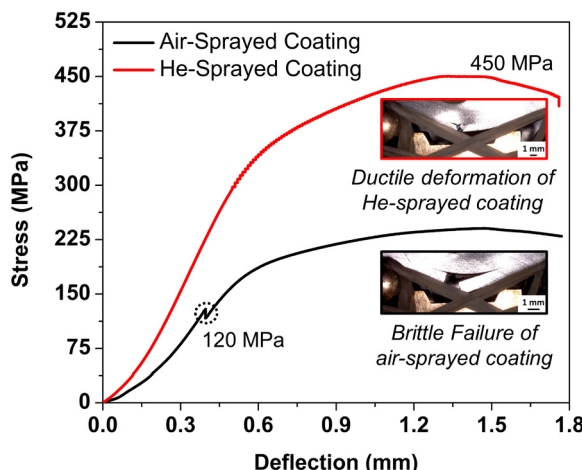


Fig. 4. Flexural stress-displacement plot comparing deformation of Air-processed and He-processed coatings. The insets show the optical images of the failed and delaminated specimens.

separate opposing direction strain contours is much lower for y-direction deformation. The anisotropy in the deformation behavior of splats and splat interfaces is related to the coating microstructure. He-sprayed particles undergo significant plastic deformation (Figs. 2b and 3b), with a mean particle flattening ratio of 1.6. The particles also display prominent jetting, as shown in Fig. 2d. Jetting leads to the formation of metallurgical bond in the peripheral/ outer boundary of the particle due to the removal of surface oxides and the exposure of a clean metal surface [22]. However, the particle boundary which directly impacts on the substrate/ coating during cold spray is not metallurgically bonded

and rather experiences significant cold working characterized by high density of dislocations [22,27,35]. This results in varying degree of inter-splat bonding, which is location specific. The anticipated variation of inter-splat bonding is marked on an SEM micrograph in Fig. 6d. It can be seen that strong metallurgical bonding along the periphery of the splat will restrict deformation along the y-axis (or the spraying direction). On the other hand, the absence of jetting at the point of particle impact will result in weak bonding, and hence the horizontal interface is susceptible to de-bonding, delamination and relative sliding upon the application of load. This explains the remarkable degree of anisotropy observed in the microstrains.

Since microstructure deformation is more pronounced in x-direction (perpendicular to spray direction), the x-strains of air-processed and He-processed coatings are compared in Fig. 7. The air-sprayed coating is characterized by a higher residual strain at the end of one cycle ($\sim 1 \mu\text{m}/\text{m}$) as compared to He-sprayed coating ($0.2 \mu\text{m}/\text{m}$). The He-sprayed coating also exhibits a reversible plastic deformation behavior. The absolute value of strains remains same when the dynamic loading direction is reversed. This is in contrast to the air-sprayed coating, where changing the direction of applied load amplitude only marginally reverses the microstructure strain direction. This suggests the nature of inter-splat deformation is more ductile for He-sprayed coating. To understand the plastic vs. brittle deformation behavior, it is important to look into the variables that affect yield strength (σ_{YS}) of the material [36]:

$$\sigma_{YS} = \sigma_m + \sigma_{SS} + \sigma_{GB} + \sigma_d + \sigma_p \quad (1)$$

where σ_m , σ_{SS} , σ_{GB} , σ_d and σ_p are the contribution of the metal matrix, solid solution, grain boundary hardening, dislocations and the particle inclusions. During particle impact in cold spray, oxide shell is fragmented and pushed out due to interfacial shear stress. However, some of the oxide fragments are accumulated at splat interfaces [34]. Therefore, the

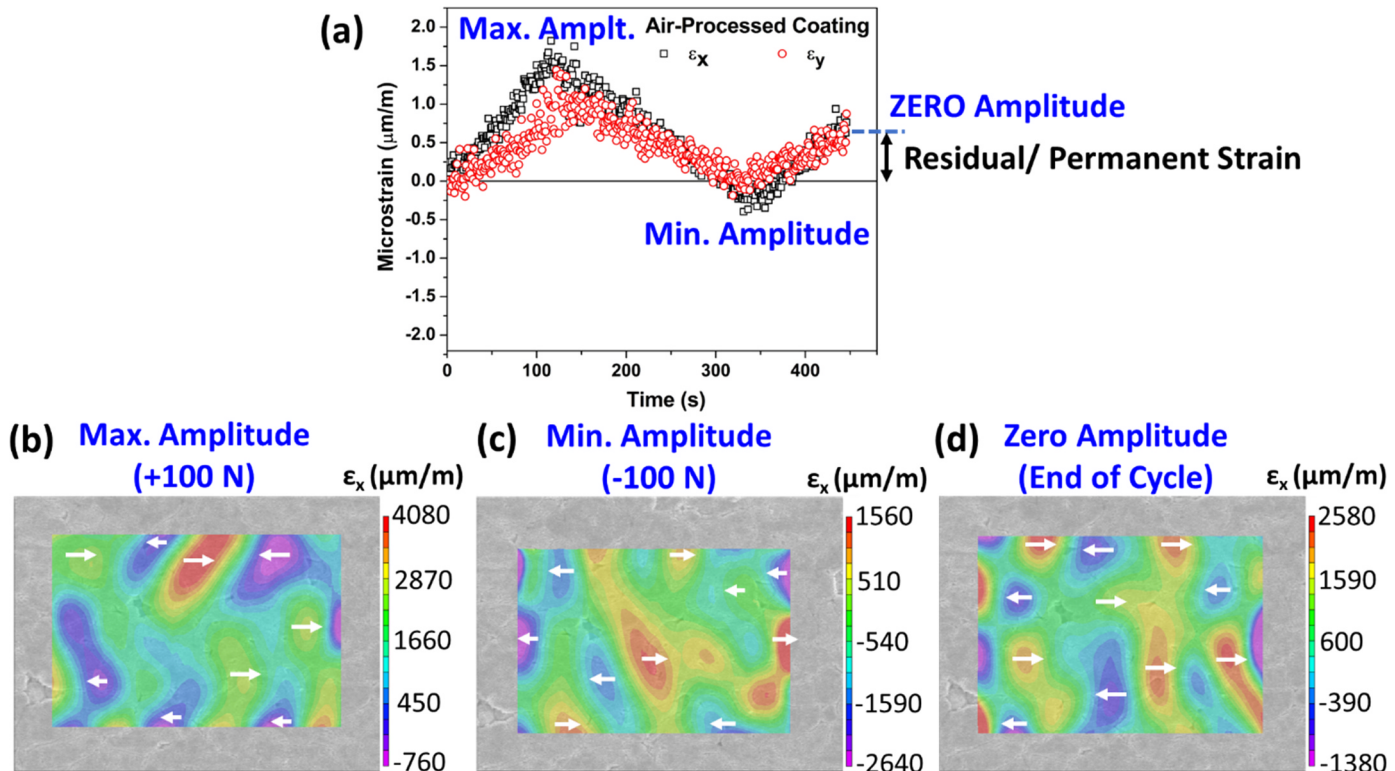


Fig. 5. (a) Microstructure strain evolution during a load cycle for an Air-processed coating obtained by Digital Image Correlation (DIC) Analysis. Strains in x and y directions are compared to assess the degree of anisotropy. The DIC maps showing strain contours at different load amplitudes during the cyclic deformation are compared: (b) maximum amplitude of $+100 \text{ N}$, (c) minimum amplitude of -100 N , and (d) ZERO load amplitude at the end of the loading cycle. The direction of the white arrows indicate positive and negative-direction local strains, implying relative sliding between splats in the microstructure during deformation. The image width in b-d is $190 \mu\text{m}$.

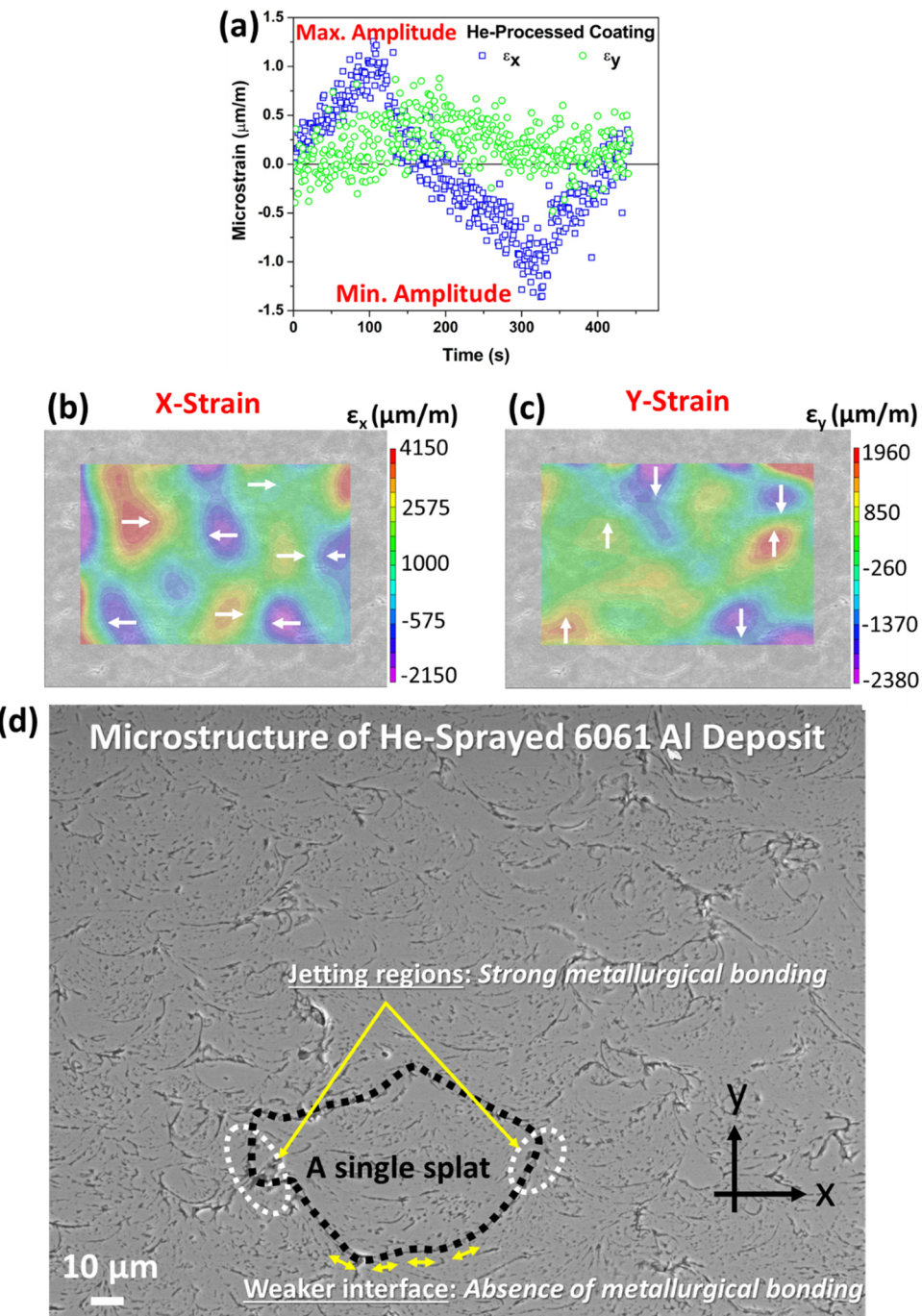


Fig. 6. (a) Microstructure strain evolution during a load cycle for the He-processed coating obtained by DIC Analysis. A marked difference in the microstructure strains in x and y-directions reveals a high degree of anisotropy. A comparison of DIC strain maps is shown for: (b) x-direction strains, and (c) y-direction strains. The image width in b, c is 190 μm . (d) Representation of the varying degree of particle-particle bonding along different locations of splat boundary, responsible for anisotropic strains.

splat boundaries can be locally treated as nanocomposites of Al alloy containing Al_2O_3 particles. Al_2O_3 debris can obstruct dislocation motion in the metal splat and thereby enhance the yield stress. The strengthening effect due to oxide particles can be expressed as [36]:

$$\sigma_p = M \Delta \tau \quad (2)$$

where M is Taylors factor, and $\Delta \tau$ is the increase in stress required to shear the material. For the plastic yielding of splat to occur, the applied stress must be able to deform the matrix as well as the particles. This shear stress is given as [37]:

$$\Delta \tau_{\text{Ansell-Lenel}} = \frac{2}{3} \frac{G}{4C} \left(\frac{f^{1/3}}{0.82 - f^{1/3}} \right) \quad (3)$$

where f is the volume fraction of the particles, G is the shear modulus, and C is a material constant. The higher volume fraction of oxide inclusions (f) along the splat interfaces will enhance the resistance to plastic flow. It is well-known that some degree of particle oxidation occurs during cold spray [38]. With air as the process gas, the in-flight oxidation of the alloy particles will be higher compared to the particles sprayed using He gas. Therefore, the splat interfaces in air-sprayed coating will have more oxide inclusions (higher value of ' f ' in Eq. (3)).

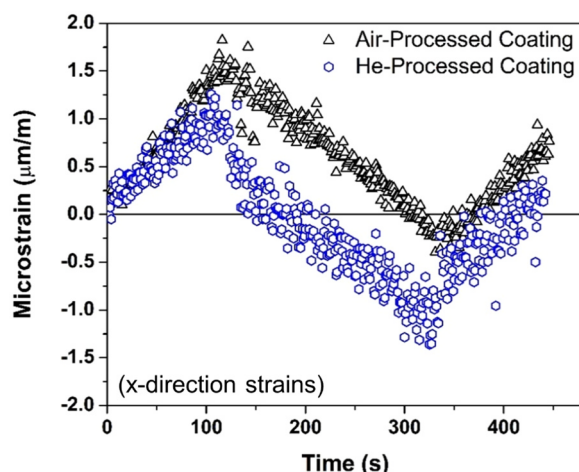


Fig. 7. A comparative plot of microstructure strains in x-direction in Air and He-processed coatings.

Consequently, the local yield stress (at the interfaces) will be higher for air-sprayed coating, limiting the scope for plastic deformation. Non-plastic deformation, such as inter-splat de-bonding during deformation is more likely to be active. The de-bonded interfaces cannot slide back to their original configuration easily, resulting in poor reversibility of microstrains and high permanent residual strain for air-sprayed coating, as observed by DIC analysis.

In addition to the oxide, inter-splat porosity also contributes towards poor ductility of the air-sprayed coating. The strain evolution at a dense single splat site was compared with a porous location using DIC. Supplementary Video V5 compares the strain evolution at a porous site and dense splats. It can be observed that a high degree of strain fluctuation occurs at the pore. The standard deviation of local strains at the porous site (marked in the video) was computed to be 4.29×10^{-4} , which is an order of magnitude higher than the standard deviation of local strains for a dense splat ($\sim 8.1 \times 10^{-5}$). This suggests that porous splat interfaces are sites of inter-splat sliding due to poor particle-particle bonding. Therefore, improving coating density and healing inter-splat porosities is vital to improve mechanical properties.

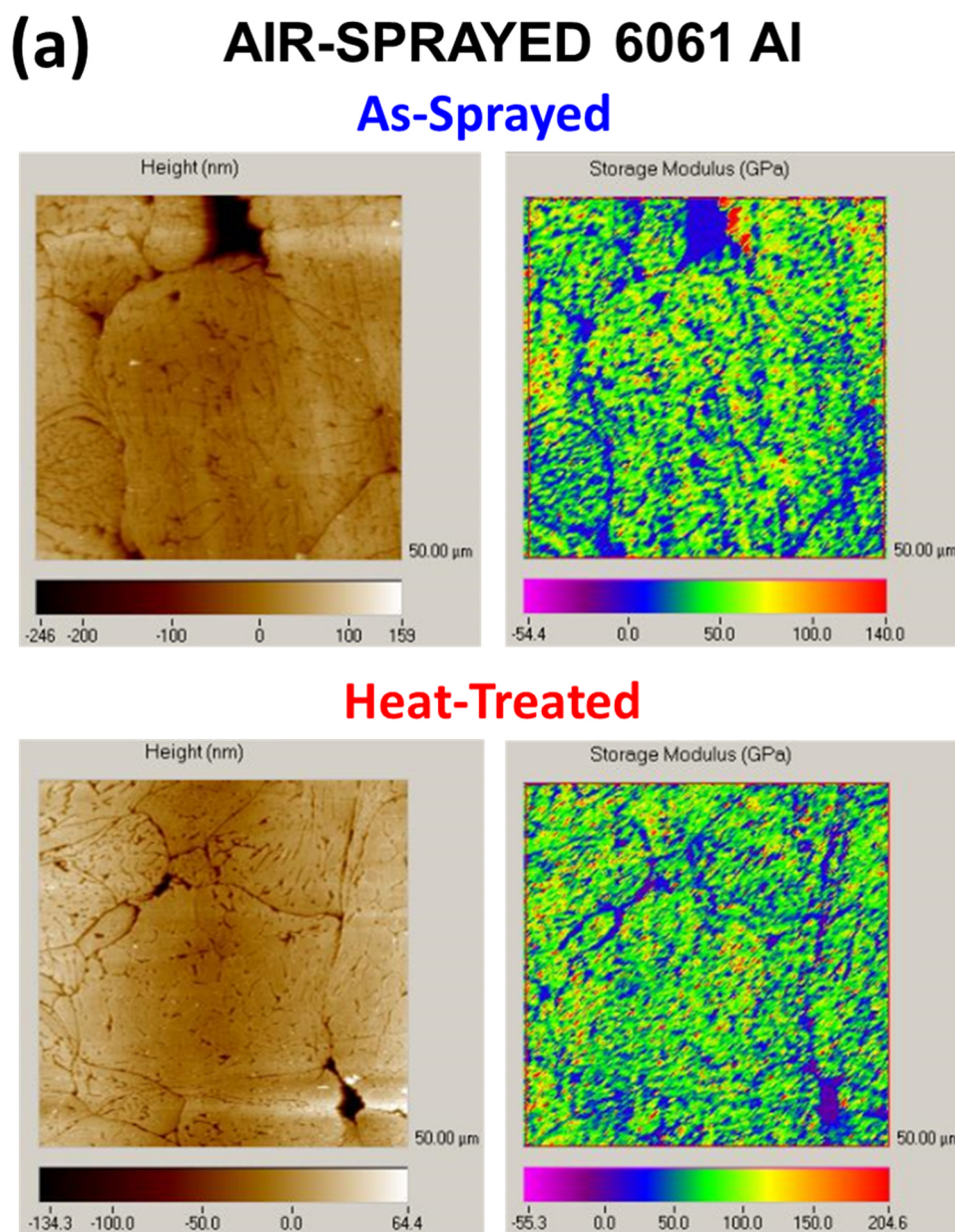
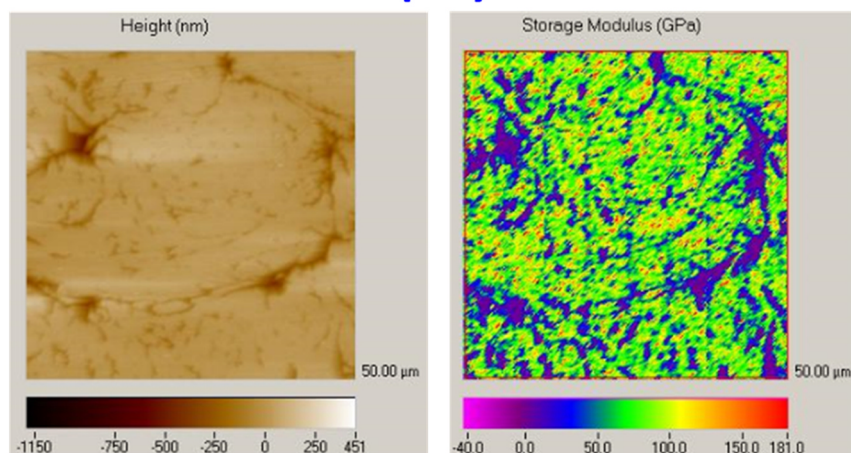


Fig. 8. Scanning probe microscopy surface topography imaging and corresponding nanoindentation modulus maps for 6061 Al coatings for: (a) air-sprayed, and (b) He-sprayed coatings in as-sprayed and heat-treated conditions. The colored contours in the maps represent local modulus distribution.

(b) HELIUM-SPRAYED 6061 Al

As-Sprayed



Heat-Treated

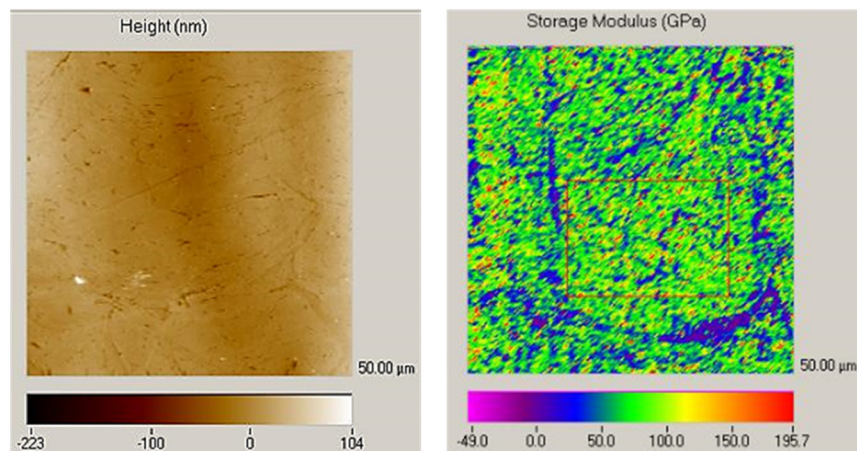


Fig. 8. (continued)

3.2.3. Effect of heat treatment on splat structure & mechanical properties

Both air-sprayed and He-sprayed coatings were heat-treated and SPM imaging of the etched coating cross-section was performed to gather precise information about splat structure and splat interfaces in the coatings (Fig. 8). Air-sprayed coating was characterized by large inter-splat porosities (Fig. 8a). Contrary to this, splat boundaries in Helium-sprayed coating exhibit significantly arrested porosity (Fig. 8b). This was confirmed by modulus mapping of the corresponding regions: blue colored regions with ~zero/ extremely low modulus values represent porosity in the coating (Fig. 8). Upon heat-treatment, both the coatings show reduction in porosity. Solid state diffusion during heat-treatment aids in coalescence of voids [39], healing the micro-cracks between the splats. This is also evident from the modulus maps, as the blue colored contours are much finer in heat-treated coatings. Inter-splat crack healing at elevated temperature can be hypothesized to proceed via a 3-step diffusion process [40]: (i) chemical potential gradient between the edge and center of the crack induces surface diffusion to form a doughnut-shaped channel pore along the outer edge of the crack, (ii) this doughnut-shaped pore splits to form spherical voids due to Rayleigh instabilities, and (iii) shrinkage of these spherical pores leads to microstructure densification (Fig. 8).

As a result of arrested porosity and denser microstructure, heat-treated coatings were characterized with higher microhardness,

compared to as-sprayed coatings (Fig. 9). Weak particle-particle interfaces can de-bond due to indentation-induced stresses during micro-hardness testing [26]. This activates splat sliding, compromising the

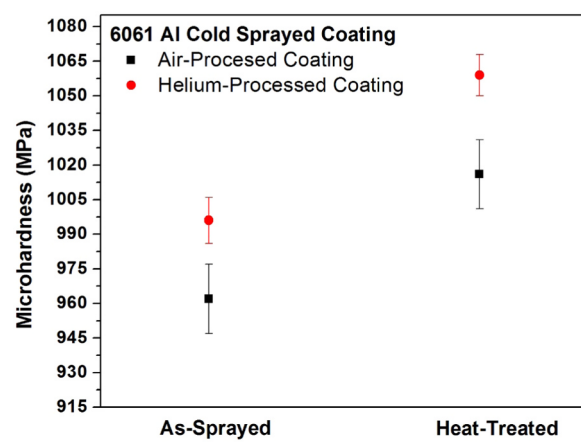


Fig. 9. Average microhardness of 6061 Al coatings in as-sprayed and heat-treated conditions.

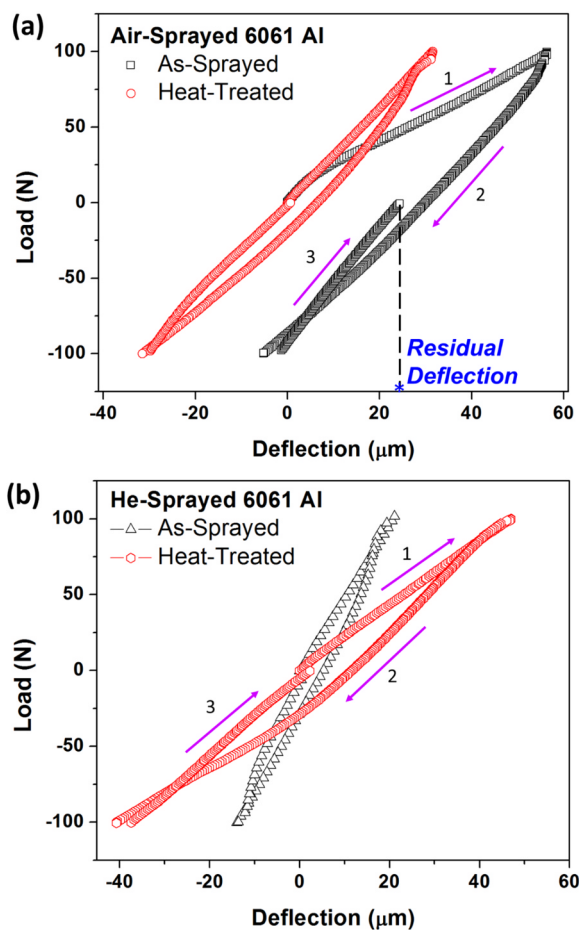


Fig. 10. Load-deflection plots for cyclic flexural response of cold-sprayed coatings before and after heat-treatment for: (a) air-sprayed coating, and (b) He-sprayed coating. Segments 1, 2 and 3 represent loading, unloading and re-loading regimes, respectively.

resistance to plastic deformation [25]. Heat-treated coatings show superior resistance to indentation, evidenced by $\sim 5\text{--}7\%$ improvement in microhardness. During heat-treatment, individual splats undergo thermal expansion (Aluminum is characterized by a high thermal expansion coefficient $\sim 26.5 \times 10^{-6} \text{ K}^{-1}$ at 200°C [41]), resulting in thermal ‘compressive’ stress [42] along splat boundaries. This inter-splat compression produces intimate contact, aiding in enhanced diffusion. As a result, metallurgical bonding is created along the mechanically interlocked interfaces [43,44]. Metallurgically bonded interfaces resist splat sliding, improving the overall microhardness of the coatings.

The heat-treated coatings were subjected to 4-point bending cyclic loading-unloading-reloading cycle inside the SEM and the real-time videos were recorded. Loading conditions used were identical to as-sprayed coatings. The load-deflection profiles for the coatings before and after heat-treatment are compared in Fig. 10. The segments 1, 2 and 3 marked in the F-h plots represent loading, unloading and re-loading regimes, respectively. At peak load amplitude of $+100 \text{ N}$, air-sprayed coating experienced a deflection exceeding $50 \mu\text{m}$ (Fig. 10a). However, the deflection for heat-treated coating (air-processed) was significantly arrested ($\sim 30 \mu\text{m}$). Air-sprayed coating prior to heat-treatment was also characterized by a ‘residual’ deflection ($\sim 24 \mu\text{m}$) at the end of the cycle, indicating inferior resistance to plastic deformation. However, heat-treated coating had minimal residual deformation ($< 0.7 \mu\text{m}$) (Fig. 10a). This suggests splat sliding in heat-treated coating is restricted. Additionally, it was noticed that even after the direction of loading was reversed, the deflection was predominantly

positive for the as-sprayed coating during the deformation cycle. This is indicative of greater irreversible deformation. The weak interfaces debond and the splats slide past each other, causing energy dissipation and poor mechanical recovery. However, the heat-treated coating demonstrated negative displacement when the direction of loading was reversed (Fig. 10a), which can be attributed to superior bonding.

He-sprayed coating demonstrated excellent resistance to plastic deformation even before heat-treatment, as evidenced from the cyclic F-h plot in Fig. 10b. The maximum deflection at $+100 \text{ N}$ load amplitude was recorded to be $\sim 20 \mu\text{m}$. It is noteworthy that severe plastic deformation of particles during cold spray result in excessive residual stresses, limiting the plasticity of the coating. Heat-treatment relieves the residual stress and enhances the plasticity, as seen from comparative F-h plot in Fig. 10b. The maximum deflection at peak load was found to be exceeding $45 \mu\text{m}$. Nevertheless, the overall resistance to plastic deformation was excellent even after heat treatment, evidenced from negligible residual deflection after the load amplitude was ZERO at the end of the cycle (Fig. 10b).

DIC analysis of the real-time snapshots was performed to decipher microstructure strain evolution in the heat treated coatings. The net microstructure strain evolution (during 1 cycle) in air-sprayed coating before and after heat-treatment is compared in Fig. 11a. The heat-treated coating exhibited superior plasticity: it showed negative microstructure strains when the direction of loading was reversed. Contrary to this, the as-sprayed coating demonstrated minimal negative strain and a permanent residual strain at the end of the cycle. The strain maps at peak load amplitude ($+100 \text{ N}$) before and after heat-treatment are compared in Fig. 11b. It is seen that the local plasticity of individual splats is significantly enhanced: the maximum local strain contour value was found to be $\sim 11,400 \mu\text{m/m}$ in the heat-treated microstructure, as opposed to a peak local strain of $\sim 4080 \mu\text{m/m}$ for as-sprayed coating. Heat treatment induced bonding between the splats allows for effective load transfer, resulting in improved plasticity. The stress distribution is vital to prevent local crack initiation at splat interfaces upon mechanical loading. Therefore, in heat treated coatings, the interface de-bonding is prevented and as a result splat sliding is arrested. This results in arrested residual deformation/ strain as observed from Figs. 10a and 11a. This finding establishes that splat sliding is indeed responsible for relatively inferior mechanical properties of cold sprayed coatings, compared to their bulk counterparts.

Notably, DIC strain analysis of He-sprayed coating showed remarkably arrested anisotropy in microstructure deformation, observed by comparing microstructure strains in x (ε_x) and y-directions (ε_y) (Fig. 12a). As stated before, metallurgical bonding in cold-sprayed coatings is in general confined to the regions that undergo ‘jetting’, which results in anisotropic mechanical response (Fig. 6a). However, heat-treatment promotes diffusion, formation of metallurgical bonds and stress-relief. As a result, y-direction strains (ε_y) are not as restricted in heat-treated microstructure. Additionally, stress-relief also results in enhanced ductility, which manifested as higher microstructure strains at peak amplitudes as seen from Fig. 12b. A close observation of strain values at the end of the cycle in Fig. 12b shows that the heat-treated coating is characterized by an order of magnitude lower residual strain ($\sim 0.03 \mu\text{m/m}$), compared to as-sprayed microstructure ($\sim 0.22 \mu\text{m/m}$). This remarkable improvement in the resistance to permanent deformation is because of improved splat bonding and restricted splat sliding.

3.2.4. Correlating cold-sprayed microstructure deformation with bulk material behavior

In order to develop materials with predictable mechanical properties using cold spray technique, it is important to quantify and compare the effect of splat interfaces on the overall deformation. We propose a ‘Splat Sliding Factor’ (SS_F), which takes into account the relative deformation, sliding and de-bonding of splats in the cold sprayed microstructure. To be able to characterize this factor for the coatings, we

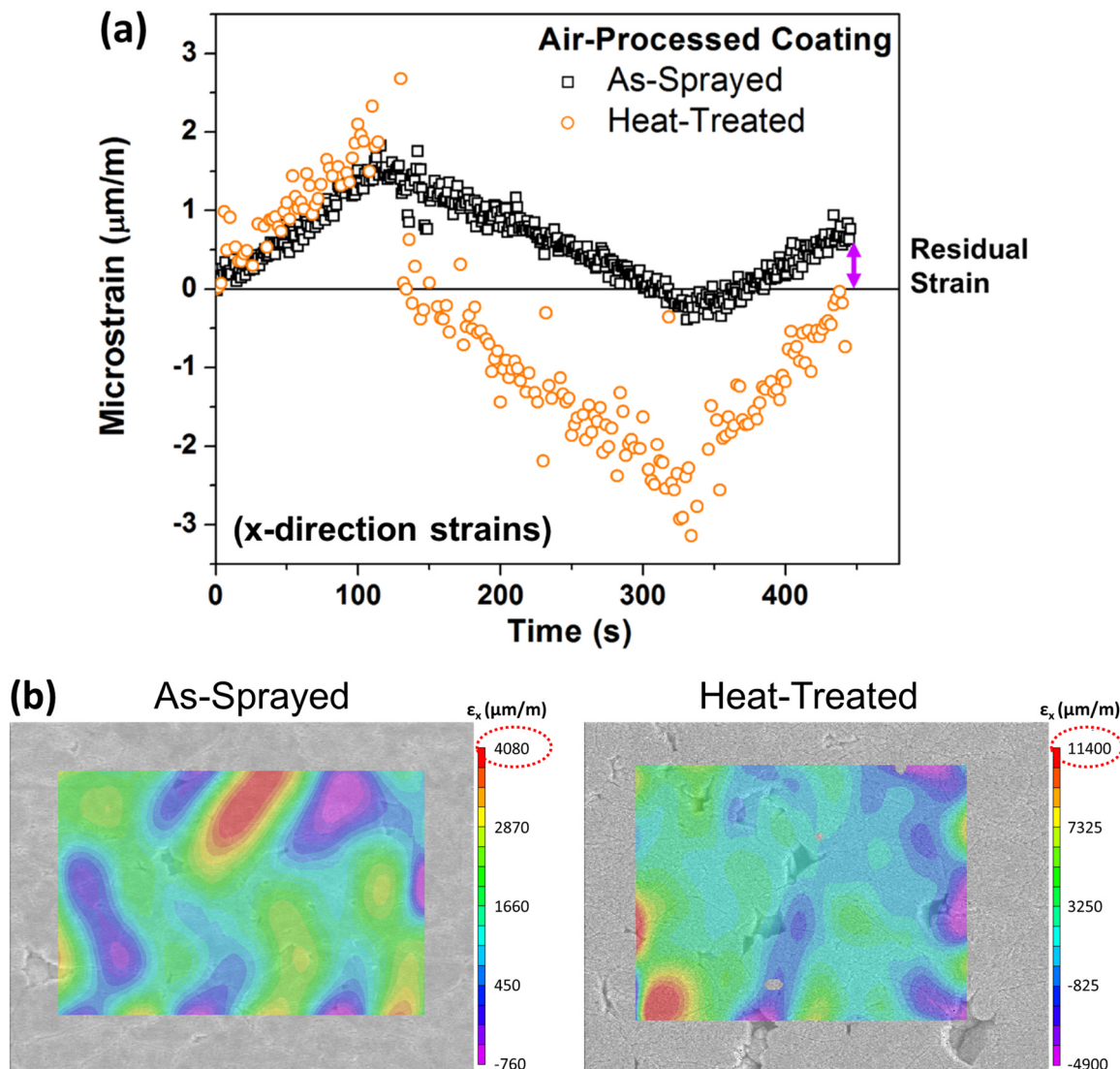


Fig. 11. DIC analysis of real-time SEM videos to determine microstructure strains in the coatings as a function of heat-treatment: (a) net x-direction microstructure strain evolution during 1 cycle, and (b) strain map at + 100 N load amplitude compared for as-sprayed and heat-treated conditions. The image width of the SEM micrographs in b is 190 μm.

performed the *in-situ* cyclic bending tests on 6061 Al-T6 substrate [45] (without coating) using the same loading conditions. The ‘residual’ strain value at the end of the cycle was determined by DIC analysis. The Splat Sliding Factor is then determined by the relation:

$$SS_f = \frac{\epsilon_i}{\epsilon_s} \quad (4)$$

where ϵ_s is the residual microstructure strain in the standard material being used as the benchmark for comparison (6061 Al-T6 substrate in this case) and ϵ_i is the residual microstructure strain in the cold sprayed coating being evaluated. ϵ_s and ϵ_i were determined from the DIC analysis of the *in-situ* videos as the final/ residual strains at the end of loading/unloading/reloading cycles for the coatings and the substrate. Since the deformation is more pronounced in the x-direction (because of tensile stress-state as shown in Fig. 1b), the factor was computed based on the x-direction strains (ϵ_x). Based on the findings in this study, this factor is dependent on microstructural attributes of the cold spray deposit:

$$SS_f = f(\text{Splat Geometry, Porosity, Interplat Bonding}) \quad (5)$$

SS_f was computed to be ~ 1.41 for air-sprayed coating and merely

~ 0.28 for He-sprayed coating. A higher SS_f value signifies accentuated inter-splat deformation or inferior splat bonding. After heat-treatment, the value of SS_f was significantly reduced (as shown in Fig. 13). The approach proposed in this study can be used to quantify the quality of particle-particle bonding during cold spray and develop process maps to predict their mechanical performance as a function of processing conditions, powder type, and post-spray heat treatment.

4. Conclusion

Inter-splat deformation characteristics in the cold sprayed 6061 Al coatings on 6061 Al-T6 substrate were probed by *in-situ* mechanical investigations. The correlation between coating microstructure and deformation behavior was examined by microhardness, flexural testing, nanoindentation, and *in-situ* testing inside SEM. Further, the effect of post-spray heat-treatment on mechanical properties and deformation mechanisms was also probed. The key findings are listed below:

- It is demonstrated in real time that cold-sprayed microstructures deform by relative sliding between the splats, known as splat sliding. Inter-splat deformation is greater in the air-sprayed coating

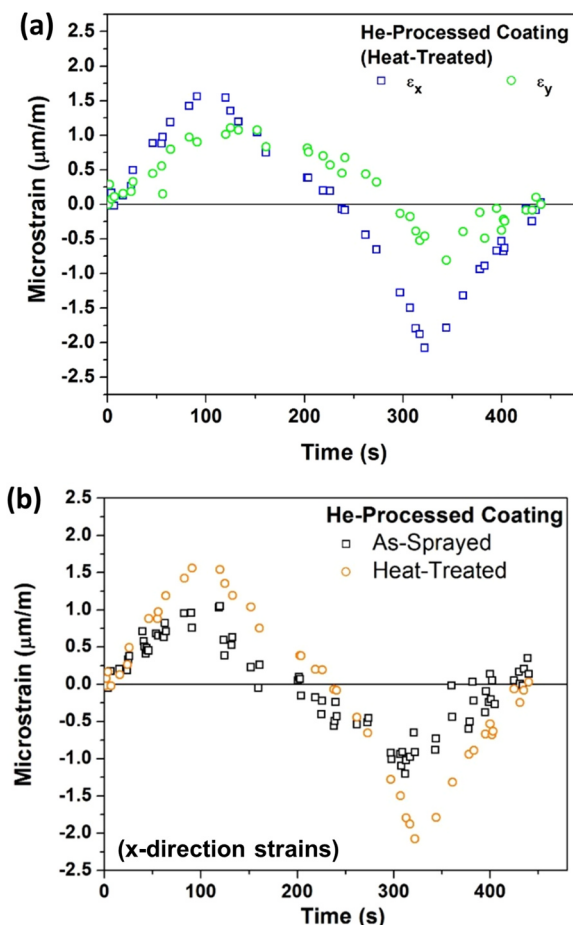


Fig. 12. Evolution of microstructure strain in He-sprayed coating during one complete loading/unloading/reloading cycle: (a) comparison of x and y-direction strain evolution after heat-treatment, and (b) comparison of x-direction strains in as-sprayed and heat-treated coatings, showing enhanced ductility after treatment.

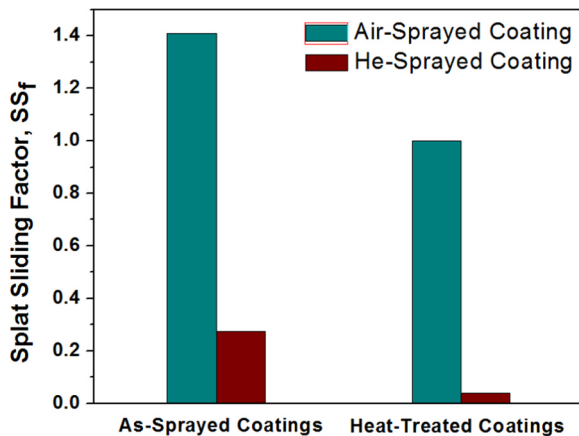


Fig. 13. Splat sliding factor compared for Air and Helium-sprayed coatings before and after heat treatment.

due to poor bonding (the permanent residual strain was 3.5 times larger than the strain in He-sprayed coating).

- Elongated splat morphology in He-sprayed coating results in high degree of anisotropy in microstructure strains, with the peak microstrain along the spraying direction only one-fourth the value of peak microstrain in the direction perpendicular to the spray direction. This is attributed to superior particle bonding along the

peripheral regions due to jetting, whereas the particle interface that directly impacts during deposition is relatively weakly bonded.

- Post-spray heat-treatment of the coatings reduces the porosity, improves inter-splat bonding and relieves residual stresses. This was evidenced by superior resistance to permanent deformation and improved isotropy of the heat-treated coatings.
- A splat sliding factor (SS_f) is proposed, that takes into account relative sliding between the splats during mechanical loading. This factor establishes a quantitative comparison of cold sprayed microstructure deformation vis-à-vis bulk, conventional microstructure. The values of SS_f were computed to be 1.41 and 0.28 for He and air-sprayed coatings, respectively. Heat-treatment resulted in lower SS_f , indicating arrested splat sliding.

The *in-situ* mechanical investigation is a powerful approach to visualize the deformation of splats and interfaces. The enhanced understanding of mechanical deformation in cold sprayed structures will enable superior processing control to develop deposits with predictable mechanical properties.

Acknowledgements

The authors thank Dr. C. A. Widener (South Dakota School of Mines & Technology, USA) for providing the cold sprayed coatings used in this study. PN, CZ, BB, and AA acknowledge the Army Research Laboratory for Grant W911NF15-2-0026 (Sub award No. 504108-78052). PN thanks Florida International University (FIU) Graduate School for the Presidential Fellowship award. Advanced Materials Engineering Research Institute (AMERI) at FIU is acknowledged for the research facilities used in this study.

Data availability

- The raw/processed data required to reproduce these findings cannot be shared at this time due to technical or time limitations.
- The raw/processed data required to reproduce these findings cannot be shared at this time as the data also forms part of an ongoing study.

References

- H. Assadi, H. Kreye, F. Gärtner, T. Klassen, Cold spraying – a materials perspective, *Acta Mater.* (2016) 382–407.
- G. Bae, Y. Xiong, S. Kumar, K. Kang, C. Lee, General aspects of interface bonding in kinetic sprayed coatings, *Acta Mater.* 56 (2008) 4858–4868.
- M.H.- Gangaraj, D. Veysset, K.A. Nelson, C.A. Schuh, In-situ observations of single micro-particle impact bonding, *Scr. Mater.* 145 (2018) 9–13.
- V. Luzin, K. Spencer, M.-X. Zhang, Residual stress and thermo-mechanical properties of cold spray metal coatings, *Acta Mater.* 59 (2011) 1259–1270.
- V.K. Champagne, The Cold Spray Materials Deposition Process: Fundamentals and Applications, CRC Press, Boca Raton, 2007.
- K. Balani, T. Laha, A. Agarwal, J. Karthikeyan, N. Munroe, Effect of carrier gases on microstructural and electrochemical behavior of cold-sprayed 1100 aluminum coating, *Surf. Coat. Technol.* 195 (2005) 272–279.
- D. Lahiri, P.K. Gill, S. Scudino, C. Zhang, V. Singh, J. Karthikeyan, N. Munroe, S. Seal, A. Agarwal, Cold sprayed aluminum based glassy coating: synthesis, wear and corrosion properties, *Surf. Coat. Technol.* 232 (2013) 33–40.
- R.C. Dykhuisen, M.F. Smith, D.L. Gilmore, R.A. Neiser, X. Jiang, S. Sampath, Impact of high velocity cold spray particles, *J. Therm. Spray. Technol.* 8 (1999) 559–564.
- S.V. Klinkov, V.F. Kosarev, Measurements of cold spray deposition efficiency, *J. Therm. Spray. Technol.* 15 (2006) 364–371.
- V.K. Champagne, D.J. Helfritch, S.P.G. Dinavahi, P.F. Leyman, Theoretical and experimental particle velocity in cold spray, *J. Therm. Spray. Technol.* 20 (2011) 425–431.
- T. Stoltenhoff, F. Zimmermann, LOXplate® coatings for aluminum aerospace components exposed to high dynamic stresses, Praxair Surface Technologies GmbH, Ratingen, Germany.
- M. Grujicic, C.L. Zhao, W.S. DeRosset, D. Helfritch, Adiabatic shear instability based mechanism for particle/substrate bonding in the cold-gas dynamic-spray process, *Mater. Des.* (2004) 681–688.
- H. Assadi, F. Gärtner, T. Stoltenhoff, H. Kreye, Bonding mechanism in cold gas spraying, *Acta Mater.* 51 (2003) 4379–4394.
- V.K. Champagne, D. Helfritch, P. Leyman, S.G. Ahl, B. Klotz, Interface material

- mixing formed by the deposition of copper on aluminum by means of the cold spray process, *J. Therm. Spray. Technol.* 14 (2005) 330–334.
- [15] W.-Y. Li, C. Zhang, X. Guo, C.-J. Li, H. Liao, C. Coddet, Study on impact fusion at particle interfaces and its effect on coating microstructure in cold spraying, *Appl. Surf. Sci.* 254 (2007) 517–526.
- [16] M.R. Rokni, C.A. Widener, V.R. Champagne, Microstructural evolution of 6061 Aluminum gas-atomized powder and high-pressure cold-sprayed deposition, *J. Therm. Spray. Technol.* 23 (2014) 514–524.
- [17] K. Kang, J. Won, G. Bae, S. Ha, C. Lee, Interfacial bonding and microstructural evolution of Al in kinetic spraying, *J. Mater. Sci.* 47 (2012) 4649–4659.
- [18] M.R. Rokni, C.A. Widener, O.C. Ozdemir, G.A. Crawford, Microstructure and mechanical properties of cold sprayed 6061 Al in as-sprayed and heat treated condition, *Surf. Coat. Technol.* 309 (2017) 641–650.
- [19] Q. Wang, N. Birbilis, M.-X. Zhang, Interfacial structure between particles in an aluminum deposit produced by cold spray, *Mater. Lett.* 65 (2011) 1576–1578.
- [20] Y. Zou, D. Goldbaum, J.A. Szpunar, S. Yue, Microstructure and nanohardness of cold-sprayed coatings: electron backscattered diffraction and nanoindentation studies, *Scr. Mater.* 62 (2010) 395–398.
- [21] M.R. Rokni, C.A. Widener, G.A. Crawford, M.K. West, An investigation into microstructure and mechanical properties of cold sprayed 7075 Al deposition, *Mater. Sci. Eng. A* 625 (2015) 19–27.
- [22] D. Goldbaum, R.R. Chromik, S. Yue, E. Irissou, J.-G. Legoux, Mechanical property mapping of cold sprayed Ti splats and coatings, *J. Therm. Spray. Technol.* 20 (2011) 486–496.
- [23] A. Loganathan, S. Rengifo, A.F. Hernandez, Y. Emirov, C. Zhang, B. Boesl, J. Karthikeyan, A. Agarwal, Effect of 2D WS₂ addition on cold-sprayed aluminum coating, *J. Therm. Spray. Technol.* 26 (2017) 1585–1597.
- [24] S.R. Bakshi, D. Wang, T. Price, D. Zhang, A.K. Keshri, Y. Chen, D.G. McCartney, P.H. Shipway, A. Agarwal, Microstructure and wear properties of aluminum/aluminum-silicon composite coatings prepared by cold spraying, *Surf. Coat. Technol.* 204 (2009) 503–510.
- [25] F. Tang, J.M. Schoenung, Evolution of young's modulus of air plasma sprayed yttria-stabilized zirconia in thermally cycled thermal barrier coatings, *Scr. Mater.* 54 (2006) 1587–1592.
- [26] Y. Chen, S.R. Bakshi, A. Agarwal, Intersplat friction force and splat sliding in a plasma-sprayed aluminum alloy coating during nanoindentation and micro-indentation, *ACS Appl. Mater. Interfaces* 1 (2009) 235–238.
- [27] K. Balani, A. Agarwal, S. Seal, J. Karthikeyan, Transmission electron microscopy of cold sprayed 1100 aluminum coating, *Scr. Mater.* 53 (2005) 845–850.
- [28] S.R. Bakshi, T. Laha, K. Balani, A. Agarwal, J. Karthikeyan, Effect of carrier gas on mechanical properties and fracture behavior of cold sprayed aluminum coatings, *Surf. Eng.* 23 (2007) 18–22.
- [29] S.B. Pitchuka, B. Boesl, C. Zhang, D. Lahiri, A. Nieto, G. Sundararajan, A. Agarwal, Dry sliding wear behavior of cold sprayed aluminum amorphous/nanocrystalline alloy coatings, *Surf. Coat. Technol.* 238 (2014) 118–125.
- [30] A.C. Hall, D.J. Cook, R.A. Neiser, T.J. Roemer, D.A. Hirschfeld, The effect of a simple annealing heat treatment on the mechanical properties of cold-sprayed aluminum, *J. Therm. Spray. Technol.* 15 (2006) 233–238.
- [31] L. Fontoura, P. Nautiyal, A. Loganathan, B. Boesl, A. Agarwal, Nacre-inspired graphene/metal hybrid by in-situ cementation reaction and joule heating, *Adv. Eng. Mater.* (2018), <https://doi.org/10.1002/adem.201800518>.
- [32] P. Nautiyal, M. Mujawar, B. Boesl, A. Agarwal, In-situ mechanics of 3D graphene foam based ultra-stiff and flexible metallic metamaterial, *Carbon* 137 (2018) 502–510.
- [33] L. Embrey, P. Nautiyal, A. Loganathan, A. Idowu, B. Boesl, A. Agarwal, 3D graphene foam induces multifunctionality in epoxy nanocomposites by simultaneous improvement in mechanical, thermal and electrical properties, *ACS Appl. Mater. Interfaces* 9 (2017) 39717–39727.
- [34] K. Kang, S. Yoon, Y. Ji, C. Lee, Oxidation dependency of critical velocity for aluminum feedstock deposition in kinetic spraying process, *Mater. Sci. Eng. A* 486 (2008) 300–307.
- [35] C. Borchers, F. Gärtner, T. Stoltenhoff, H. Kreye, Microstructural bonding features of cold sprayed face centered cubic metals, *J. Appl. Phys.* 96 (2004) 4288–4292.
- [36] L. Parashkevova, N. Bontcheva, V. Babakov, Analytical modeling of nanocomposite stiffness, in: V. Kavardjikov, L. Parashkevova, A. Baltov (Eds.), *Mechanics of Nanomaterials and Nanotechnology*, Institute of Mechanics-BAS, 2012, pp. 93–132.
- [37] G.S. Ansell, F.V. Lenel, Criteria for yielding of dispersion-strengthened alloys, *Acta Mater.* 8 (1960) 612–616.
- [38] K. Kim, S. Kuroda, M. Watanabe, R. Huang, H. Fukunuma, H. Katanoda, Comparison of oxidation and microstructure of warm-sprayed and cold-sprayed titanium coatings, *J. Therm. Spray. Technol.* 21 (2012) 550–560.
- [39] W.-Y. Li, C.-J. Li, H. Liao, Effect of annealing treatment on the microstructure and properties of cold-sprayed Cu coating, *J. Therm. Spray. Technol.* 15 (2006) 206–211.
- [40] H.L. Zhang, P.Z. Huang, J. Sun, H. Gao, Morphological healing evolution of penny-shaped fatigue microcracks in pure iron at elevated temperatures, *Appl. Phys. Lett.* 85 (2004) 1143–1145.
- [41] A.J.C. Wilson, The thermal expansion of aluminum from 0° to 650°C, *Proc. Phys. Soc.* 53 (1941) 235–244.
- [42] Z. Yizhou, Z. You, H. Guanhui, Z. Benlian, The healing of quenched crack in 1045 steel under electropulsing, *J. Mater. Res.* 16 (2001) 17–19.
- [43] J.W. Murray, M.V. Zuccoli, T. Husain, Heat treatment of cold-sprayed C355 Al for repair: microstructure and mechanical properties, *J. Therm. Spray. Technol.* 27 (2018) 159–168.
- [44] F. Gärtner, T. Stoltenhoff, J. Voyer, H. Kreye, S. Riekehr, M. Koçak, Mechanical properties of cold-sprayed and thermally sprayed copper coatings, *Surf. Coat. Technol.* 200 (2006) 6770–6782.
- [45] Heat treating of Aluminum alloys, *ASM Handbook*, Vol 4, ASM International, 1991, pp. 841–879.